

MODELS OF LOW MASS STARS

A Thesis
Submitted to the Faculty
in partial fulfillment of the requirements for the
degree of

Doctor of Philosophy

in
Physics and Astronomy
by Emily M. Boudreaux

Guarini School of Graduate and Advances Studies
Dartmouth College
Hanover, New Hampshire

April 2024

Examining Committee:

(chair) ***Brian C. Chaboyer***

Elisabeth R. Newton

Aaron Dotter

Gregory Feiden

F. Jon Kull, Ph.D.
Dean of the Guarini School of Graduate and Advanced Studies

Copyright Notice

This work is licensed under the Creative Commons
Attribution-NonCommercial-ShareAlike 4.0 International License.

To view a copy of this license, visit

<http://creativecommons.org/licenses/by-nc-sa/4.0/>

or send a letter to

Creative Commons, PO Box 1866, Mountain View, CA 94042, USA.

For Poppy, who taught me to build and supported as I did.

Abstract

Low mass stars account for approximately 70 percent of the stellar populations; yet, due to their small sizes and cool temperatures they account for only **NUMBER** percent of the galaxies luminosity function. Consequently, across multiple domains there has been a dearth of interest in these key astronomical objects. In this thesis I present two projects which have further revealed properties of low mass stars. Firstly, I present chemically self consistent models of the globular clusters NGC 2808 and NGC 6752. Due to the ages of both clusters, these models are dominated by low mass stars. We find that chemical consistency between a stars structural and atmospheric models makes only a trivial difference in model predictions. Secondly, I present a detailed investigation into the Gaia M Dwarf Gap (the Jao Gap) looking at how the Jao Gap's theoretical location is effected by high temperature radiative opacity source and how the physics which drives the Jao Gap's formation may also drive perturbations to stellar magnetic field strength.

Preface

This work was conducted under the supervision of Brian Chaboyer and I would not have been able to complete this thesis without his continued support. I would like to thank Brian immensely for his continued support and for being a wonderful teacher. Further, I am more grateful than words can express for the love and support which my parents, Karol and Don, have provided me throughout my entire life. They have guided, cared, and loved me from the day I told them I was going to be an astronomer in pre-school to the day I defend this thesis. Finally, I would like to thank my friends for always being there for me and for making graduate school both fun and an incredible learning experience.

Contents

| | | |
|----------|--|-----------|
| 1 | Introduction | 1 |
| 2 | Globular Clusters | 3 |
| 2.1 | Why Globular Clusters Matter | 3 |
| 2.2 | Modeling Globular Clusters | 3 |
| 2.2.1 | Problems Modeling Globular Clusters | 3 |
| 2.3 | Modeling NGC 2808 | 3 |
| 2.4 | Modeling NGC 6752 | 3 |
| 3 | Magnetic Fields In M Dwarfs | 5 |
| 3.1 | Magnetic Activity in M dwarfs | 5 |
| 3.2 | Observations & Data Reduction | 8 |
| 3.3 | Analysis | 9 |
| 3.3.1 | Rotation and Rossby Number | 12 |
| 3.4 | Rotation–Activity Relation | 13 |
| 3.5 | Magnetic Activities in M dwarfs Closing Thoughts | 19 |
| 4 | Jao Gap | 21 |
| 4.1 | Jao Gap Sensitivity to Opacity | 21 |
| 4.2 | INTRODUCTION | 21 |
| 4.3 | Jao Gap | 23 |
| 4.3.1 | Efforts to Model the Gap | 24 |
| 4.4 | Updated Opacities | 26 |
| 4.4.1 | Table Querying and Conversion | 27 |

| | | |
|----------|--|-----------|
| 4.4.2 | Solar Calibrated Stellar Models | 28 |
| 4.5 | <code>pyTOPSScrape</code> | 29 |
| 4.6 | Interpolating $\rho \rightarrow R$ | 29 |
| 4.7 | Modeling | 31 |
| 4.7.1 | Population Synthesis | 32 |
| 4.7.2 | Mixing Length Dependence | 35 |
| 4.8 | Results | 36 |
| 4.9 | Jao Gap connection to Magnetism | 40 |
| 5 | Conclusions | 41 |

List of Tables

| | | |
|-----|--|----|
| 3.1 | Calculated Rossby Numbers and R'_{HK} values. All circular data points in Figures 3.2 & 3.3 are present in this table. Masses are taken from the MEarth database. A machine readable version of this table is available | 14 |
| 4.1 | Optimized parameters for SCSMs evolved using OPAL and OPLIB high temperature opacity tables. | 29 |
| 4.2 | Locations identified as potential Gaps. | 37 |

List of Figures

| | |
|--|----|
| 4.2 Diagram for a characteristic stellar model of $0.35625 M_{\odot}$ which is within the Jao Gap's mass range. The black shaded regions denote whether, at a particular model age, a radial shell within the model is radiative (with white meaning convective). The lines trace the models core temperature, core ^3He mass fraction, fractional luminosity wrt. the zero age main sequence and fractional radius wrt. the zero age main sequence. | 25 |
| 4.3 Rosseland mean opacity with the GS98 solar composition for both OPAL opacities and OPLIB opacities (top). Residuals between OPLIB opacities and OPAL opacities (bottom). These opacities are plotted at $\log_{10}(R) = -0.5$, $X = 0.7$, and $Z = 0.02$. $\log_{10}(R) = -0.5$ approximates much of the interior a $0.35 M_{\odot}$ model. Note how the OPLIB opacities are systematically lower than the OPAL opacities for temperatures above $10^{5.2}$ K. | 27 |
| 4.4 HR Diagram for the two SCSMs, OPAL and OPLIB. OPLIB is shown as a red dashed line. | 28 |
| 4.5 Log Fractional Difference between opacities in $\kappa_R(\rho, T_{eff})$ space directly queried from the OPLIB web-form and those which have been interpolated into $\log(R)$ space and back. Note that, due to the temperature grid of type 1 OPAL tables not aligning perfectly with the temperature grid OPLIB uses there may be edge effects where the interpolation is poorly constrained. The red line corresponds to $\log(R) = -0.79$ where much of a stellar model's radius exists. | 31 |
| 4.6 Mass-luminosity relation at 7 Gyrs for models evolved using OPAL opacity tables (top) and those evolved using OPLIB opacity tables (bottom). Note the lower mass range of the OPLIB Gap. | 32 |
| 4.7 Probability distribution sampled when assigning true parallaxes to synthetic stars. This distribution is built from the GCNS and includes all stars with BP-RP colors between 2.3 and 2.9, the same color range of the Jao Gap. | 33 |

Chapter 1

Introduction

Chapter 2

Globular Clusters

2.1 Why Globular Clusters Matter

2.2 Modeling Globular Clusters

2.2.1 Problems Modeling Globular Clusters

2.3 Modeling NGC 2808

2.4 Modeling NGC 6752

Chapter 3

Magnetic Fields In M Dwarfs

3.1 Magnetic Activity in M dwarfs

M-dwarfs are the most numerous stars in our galaxy. Some planet search campaigns have focused on M-dwarfs due to the relative ease of detecting small planets in their habitable zones (e.g. ?); however, spun-up M-dwarfs are more magnetically active when compared to larger and hotter stars (???). The increase in activity may accelerate the stripping of an orbiting planet’s atmosphere (e.g. ?), and may dramatically impact habitability (?). Therefore, it is essential to understand the magnetic activity of M-dwarfs in order to constrain the potential habitability and history of the planets that orbit them. Additionally, rotation and activity may impact the detectability of hosted planets (e.g. ???).

Robust theories explaining the origin of solar-like magnetic fields exist and have proven extensible to other regions of the main sequence (?). The classical $\alpha\Omega$ dynamo relies on differential rotation between layers of a star to stretch a seed poloidal field into a toroidal field (??). Magnetic buoyancy causes the toroidal field to rise through the star. During this rise, turbulent helical stretching converts the toroidal field back into a poloidal field (?). Seed fields may originate from the stochastic movement of charged particles within a star’s atmospheres.

In non-fully convective stars the initial conversion of the toroidal field to a poloidal field is believed to take place at the interface layer between the radiative and convective regions of a star — the tachocline (???). The tachocline has two key properties

that allow it to play an important role in solar type magnetic dynamos: 1), there are high shear stresses, which have been confirmed by astroseismology (?), and 2), the density stratification between the radiative and convective zones serves to “hold” the newly generated toroidal fields at the tachocline for an extended time. Over this time, the fields build in strength significantly more than they would otherwise (?). This theory does not trivially extend to mid-late M-dwarfs, as they are believed to be fully convective and consequently do not contain a tachocline (?). Moreover, fully convective M-dwarfs are not generally expected to exhibit internal differential rotation (e.g. ??), though, some models do produce it (?).

Currently, there is no single accepted process that serves to build and maintain fully convective M-dwarf magnetic fields in the same way that the α and Ω processes are presently accepted in solar magnetic dynamo theory. Three-dimensional magneto anelastic hydrodynamical simulations have demonstrated that local fields generated by convective currents can self organize into large scale dipolar fields. These models indicate that for a fully convective star to sustain a magnetic field it must have a high degree of density stratification — density contrasts greater than 20 at the tachocline — and a sufficiently large magnetic Reynolds number¹.

An empirical relation between the rotation rate and the level of magnetic activity has been demonstrated in late-type stars (??). This is believed to be a result of faster rotating stars exhibiting excess non-thermal emission from the upper chromosphere or corona when compared to their slower rotating counterparts. This excess emission is due to magnetic heating of the upper atmosphere, driven by the underlying stellar dynamo. **The faster a star rotates, up to some saturation threshold, the more such emission is expected.** However, the dynamo process is not dependent solely on rotation; rather, it depends on whether the contribution from the rotational period (P_{rot}) or convective motion — parameterized by the convective overturn time scale (τ_c) — dominates the motion of a charge packet within a star. Therefore, the Rossby Number ($Ro = P_{rot}/\tau_c$) is often used in place of the rotational period as it accounts for both.

¹The Reynolds Number is the ratio of magnetic induction to magnetic diffusion; consequently, a plasma with a larger magnetic Reynolds number will sustain a magnetic field for a longer time than a plasma with a smaller magnetic Reynolds number.

The rotation-activity relation was first discovered using the ratio of X-ray luminosity to bolometric luminosity (L_X/L_{bol}) (?) and was later demonstrated to be a more general phenomenon, observable through other activity tracers, such as Ca II H&K emission (?). This relation has a number of important structural elements. ? showed that magnetic activity as a function of Rossby Number is well modeled as a piecewise power law relation including a saturated and non-saturated regime. In the saturated regime, magnetic activity is invariant to changes in Rossby Number; in the non-saturated regime, activity decreases as Rossby Number increases. The transition between the saturated and non-saturated regions occurs at $Ro \sim 0.1$ (e.g. ?). Recent evidence may suggest that, instead of an unsaturated region where activity is fully invariant to rotational period, activity is more weakly, but still positively, correlated with rotation rate (????).

Previous studies of the Ca II H&K rotation-activity relation (e.g. ?????) have focused on spectral ranges which both extend much earlier than M-dwarfs and which do not fully probe late M-dwarfs. **Other studies have relied on $v \sin(i)$ measurements (e.g. ??), which are not sensitive to the long rotation periods reached by slowly rotating, inactive mid-to-late type M dwarfs (70-150 days: ?).** Therefore, these studies can present only coarse constraints on the rotation activity relation in the fully convective regime. The sample we present in this paper is focused on mid-to-late type M dwarfs, **with photometrically measured rotational periods**, while maintaining of order the same number of targets as previous studies. Consequently, we provide much finer constraints on the rotation-activity relation in this regime.

We present a high resolution spectroscopic study of 53 mid-late M-dwarfs. We measure Ca II H&K strengths, quantified through the R'_{HK} metric, which is a bolometric flux normalized version of the Mount Wilson S-index. These activity tracers are then used in concert with photometrically determined rotational periods, compiled by ?, to generate a rotation-activity relation for our sample. This paper is organized as follows: Section 3.2 provides an overview of the observations and data reduction, Section 3.3 details the analysis of our data, and Section 4.8 presents our

results and how they fit within the literature.

3.2 Observations & Data Reduction

We **initially** selected a sample of 55 mid-late M-dwarfs from targets of the MEarth survey (?) to observe. Targets were selected based on high proper motions and availability of a previously measured photometric rotation period, or an expectation of a measurement based on data available from MEarth-South at the time. These rotational periods were derived photometrically (e.g. ???). For star 2MASS J06022261-2019447, which was categorized as an “uncertain detection” from MEarth photometry by ?, including new data from MEarth DR10 we find a period of 95 days. This value was determined following similar methodology to ? and ??, and is close to the reported candidate period of 116 days. References for all periods are provided in the machine readable version of Table 3.1.

High resolution spectra were collected from March to October 2017 using the Magellan Inamori Kyocera Echelle (MIKE) spectrograph on the 6.5 meter Magellan 2 telescope at the Las Campanas Observatory in Chile. MIKE is a high resolution double echelle spectrograph with blue and red arms. Respectively, these cover wavelengths from 3350 - 5000 Å and 4900-9500 Å (?). We collected data using a 0.75x5.00” slit resulting in a resolving power of 32700. Each science target was observed an average of four times with mean integration times per observation ranging from 53.3 to 1500 seconds. **Ca II H&K lines were observed over a wide range of signa-to-noise ratios, from ~ 5 up to ~ 240 with mean and median values of 68 and 61 respectively.**

We use the CarPy pipeline (??) to reduce our blue arm spectra. CarPy’s data products are wavelength calibrated, blaze corrected, and background subtracted spectra comprising 36 orders. We shift all resultant target spectra into the rest frame by cross correlating against a velocity template spectrum. For the velocity template we use an observation of Proxima Centauri in our sample. This spectrum’s velocity is both barycentrically corrected, using astropy’s SkyCoord module (?), and corrected for Proxima Centauri’s measured radial velocity, -22.4 km s^{-1} (?). Each echelle order

of every other target observation is cross correlated against the corresponding order in the template spectra using `specutils template correlate` function (?). Velocity offsets for each order are inferred from a Gaussian fit to the correlation vs. velocity lag function. For each target, we apply a three sigma clip to list of echelle order velocities, visually verifying this clip removed low S/N orders. We take the mean of the sigma-clipped velocities Finally, each wavelength bin is shifted according to its measured velocity.

Ultimately, two targets (2MASS J16570570-0420559 and 2MASS J04102815-5336078) had S/N ratios around the Ca II H&K lines which were too low to be of use, reducing the number of R'_{HK} measurement we can make from 55 to 53.

3.3 Analysis

Since the early 1960s, the Calcium Fraunhofer lines have been used as chromospheric activity tracers (?). Ca II H&K lines are observed as a combination of a broad absorption feature originating in the upper photosphere along with a narrow emission feature from non-thermal heating of the upper chromosphere (?). Specifically, the ratio between emission in the Ca II H&K lines and flux contributed from the photosphere is used to define an activity metric known as the S-index (?). The S-index increases with increasing magnetic activity. The S-index is defined as

$$S = \alpha \frac{f_H + f_K}{f_V + f_R} \quad (3.1)$$

where f_H and f_K are the integrated flux over triangular passbands with a full width at half maximum of 1.09 Å centered at 3968.47 Å and 3933.66 Å, respectively. The values of f_V and f_R are integrated, top hat, broadband regions. They approximate the continuum (Figure 3.1) and are centered at 3901 Å and 4001 Å respectively, with widths of 20 Å each. Finally, α is a scaling factor with $\alpha = 2.4$.

Following the procedure outlined in ? we use the mean flux per wavelength interval, \tilde{f}_i , as opposed to the integrated flux over each passband when computing the S-index. This means that for each passband, i , with a blue most wavelength $\lambda_{b,i}$ and a red

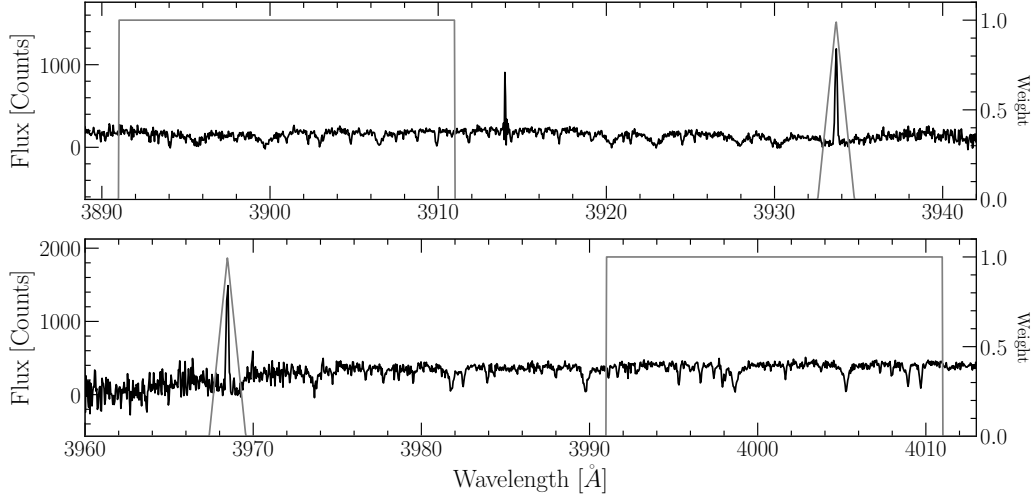


Figure 3.1: Spectrum of 2MASS J06105288-4324178 overplotted with the S index bandpasses. (top) V band and Ca II K emission line. (bottom) Ca II H emission line and R band. Note that the rectangular and triangular regions denote both the wavelength range of the band and the relative weight assigned to each wavelength while integrating.

most wavelength $\lambda_{r,i}$, \tilde{f}_i is the summation of the product of flux (f) and weight (w_i) over the passband.

$$\tilde{f}_i = \frac{\sum_{l=\lambda_{b,i}}^{\lambda_{r,i}} f(l)w_i(l)}{\lambda_{r,i} - \lambda_{b,i}} \quad (3.2)$$

where w_i represents the triangular passband for f_H & f_K and the tophat for f_V & f_R .

Additionally, the spectrograph used at Mount Wilson during the development of the S-index exposed the H & K lines for eight times longer than the continuum of the spectra. Therefore, for a modern instrument that exposes the entire sensor simultaneously, there will be 8 times less flux in the Ca II H&K passbands than the continuum passbands than for historical observations. This additional flux is accounted for by defining a new constant α_H , defined as:

$$\alpha_H = 8\alpha \left(\frac{1.09 \text{ \AA}}{20 \text{ \AA}} \right) \quad (3.3)$$

Therefore, S-indices are calculated here not based on the historical definition given in Equation 3.1; rather, the slightly modified version:

$$S = \alpha_H \frac{\tilde{f}_H + \tilde{f}_K}{\tilde{f}_V + \tilde{f}_R} \quad (3.4)$$

The S-index may be used to make meaningful comparisons between stars of similar spectral class; however, it does not account for variations in photospheric flux and is therefore inadequate for making comparisons between stars of different spectral classes. The R'_{HK} index (?) is a transformation of the S-index intended to remove the contribution of the photosphere.

R'_{HK} introduces a bolometric correction factor, C_{cf} , developed by ? and later improved upon by ?. Calibrations of C_{cf} have focused on FGK-type stars using broad band color indices, predominately B-V. However, these FGK-type solutions do not extend to later type stars easily as many mid-late M-dwarfs lack B-V photometry. Consequently, C_{cf} based on B-V colors were never calibrated for M-dwarfs as many M-dwarfs lack B and V photometry. ? provided the first C_{cf} calibrations for M-dwarfs using the more appropriate color index of $V - K$. The calibration was later extended by ?, which we adopt here.

Generally R'_{HK} is defined as

$$R'_{HK} = K\sigma^{-1}10^{-14}C_{cf}(S - S_{phot}) \quad (3.5)$$

where K is a factor to scale surface fluxes of arbitrary units into physical units; the current best value for K is taken from ?, $K = 1.07 \times 10^6 \text{ erg cm}^{-2} \text{ s}^{-1}$. S_{phot} is the photospheric contribution to the S-index; in the spectra this manifests as the broad absorption feature wherein the narrow Ca II H&K emission resides. σ is the Stephan-Boltzmann constant. If we define

$$R_{phot} \equiv K\sigma^{-1}10^{-14}C_{cf}S_{phot} \quad (3.6)$$

then we may write R'_{HK} as

$$R'_{HK} = K\sigma^{-1}10^{-14}C_{cf}S - R_{phot}. \quad (3.7)$$

We use the color calibrated coefficients for $\log_{10}(C_{cf})$ and $\log_{10}(R_{phot})$ presented in Table 1 of ?.

We estimate the uncertainty of R'_{HK} as the standard deviation of a distribution of R'_{HK} measurements from 5000 Monte Carlo tests. For each science target we offset the flux value at each wavelength bin by an amount sampled from a normal distribution. The standard deviation of this normal distribution is equal to the estimated error at each wavelength bin. These errors are calculated at reduction time by the pipeline. **The R'_{HK} uncertainty varies drastically with signal-to-noise; targets with signal-to-noise ratios ~ 5 have typical uncertainties of a few percent whereas targets with signal-to-noise ratios ~ 100 have typical uncertainties of a few tenth of a percent.**

3.3.1 Rotation and Rossby Number

The goal of this work is to constrain the rotation activity relation; therefore, in addition to the measured R'_{HK} value, we also need the rotation of the star. As mentioned, one of the selection criteria for targets was that their rotation periods were already measured; however, ultimately **6** of the 53 targets with acceptable S/N did not have well constrained rotational periods. We therefore only use the remaining 47 targets to fit the rotation-activity relation.

In order to make the most meaningful comparison possible we transform rotation period into Rossby Number . This transformation was done using the convective overturn timescale, τ_c , such that the Rossby Number, $Ro = P_{rot}/\tau_c$. To first order τ_c can be approximated as 70 days for fully-convective M-dwarfs (?). However, ? Equation (5) presents an empirically calibrated expression for τ_c . This calibration is derived by fitting the convective overturn timescale as a function of color index, in order to minimize the horizontal offset between stars of different mass in the rotation-activity relationship. The calibration from ? that we use to find convective overturn timescales and subsequently Rossby numbers is:

$$\log_{10}(\tau_c) = (0.64 \pm 0.12) + (0.25 \pm 0.08)(V - K) \quad (3.8)$$

We adopt symmetric errors for the parameters of Equation 3.8 equal to the larger of the two anti-symmetric errors presented in ? Equation 5.

3.4 Rotation–Activity Relation

We show our rotation–activity relation in Figures 3.2 & 3.3. Note that errors are shown in both figures; however, they render smaller than the data point size. Ca II H&K is also known to be time variable (e.g. ??), which is not captured in our single-epoch data. There is one target cut off by the domain of this graph, 2MASS J10252645+0512391. This target has a measured $vsini$ of $59.5 \pm 2.1 \text{ km s}^{-1}$ (?) and is therefore quite rotationally broadened, which is known to affect R'_{HK} measurements (? figure 8). The data used to generate this figure is given in Table 3.1. Table 3.1 includes uncertainties, the R'_{HK} measurements for stars which did not have photometrically derived rotational periods in MEarth, and data for 2MASS J10252645+0512391

We find a rotation activity relationship qualitatively similar to that presented in ?. Our rotation activity relationship exhibits both the expected saturated and unsaturated regimes — the flat region at $Ro < Ro_s$ and the sloped region at $Ro \geq Ro_s$ respectively. We fit the rotation activity relation given in Equation 3.9 to our data using Markov Chain Monte Carlo (MCMC), implemented in `pymc` (?).

$$\log(R'_{HK}) = \begin{cases} \log(R_s) & Ro < Ro_s \\ k \log(Ro) + \log(R_s) - k \log(Ro_s) & Ro \geq Ro_s \end{cases} \quad (3.9)$$

Ro_s is the Rossby number cutoff between the saturated and unsaturated regime. R_s is the maximum, saturated, value of R'_{HK} and k is the index of the power law when $Ro \geq Ro_s$. Due to the issues measuring R'_{HK} for high $vsini$ targets discussed above, we exclude 2MASS J10252645+0512391 from this fit. All logarithms are base ten unless another base is explicitly given.

We find best fit parameters with one σ errors:

- $k = -1.347 \pm 0.203$

| 2MASS ID | Mass M_{\odot} | Ro | $\log(R'_{HK})$ | $\log(R'_{HK})_{err}$ | V_{mag} mag | $V - K$ mag | prot d | r_{prot} |
|------------------|---------------------|-------|-----------------|-----------------------|------------------|----------------|-----------|---------------------|
| 06000351+0242236 | 0.24 | 0.020 | -4.5475 | 0.0021 | 11.31 | 5.268 | 1.809 | 2016ApJ...821...93N |
| 02125458+0000167 | 0.27 | 0.048 | -4.6345 | 0.0014 | 13.58 | 5.412 | 4.732 | 2016ApJ...821...93N |
| 01124752+0154395 | 0.28 | 0.026 | -4.4729 | 0.0017 | 14.009 | 5.240 | 2.346 | 2016ApJ...821...93N |
| 10252645+0512391 | 0.11 | 0.000 | -4.9707 | 0.0380 | 18.11 | 7.322 | 0.102 | 2016ApJ...821...93N |
| 05015746-0656459 | 0.17 | 0.873 | -5.0049 | 0.0028 | 12.2 | 5.464 | 88.500 | 2012AcA....62...67K |
| 06022261-2019447 | 0.23 | 1.307 | -5.6980 | 0.0192 | 13.26 | 4.886 | 95.000 | This Work |
| 06105288-4324178 | 0.30 | 0.705 | -5.2507 | 0.0139 | 12.28 | 4.968 | 53.736 | 2018AJ....156..217N |
| 09442373-7358382 | 0.24 | 0.542 | -5.6026 | 0.0147 | 15.17 | 5.795 | 66.447 | 2018AJ....156..217N |
| 14211512-0107199 | 0.24 | 1.160 | -5.5846 | 0.0125 | 13.12 | 5.027 | 91.426 | 2018AJ....156..217N |
| 14294291-6240465 | 0.12 | 0.394 | -5.0053 | 0.0014 | 11.13 | 6.746 | 83.500 | 1998AJ....116..429B |
| 16352464-2718533 | 0.23 | 1.423 | -5.5959 | 0.0108 | 14.18 | 5.182 | 122.656 | 2018AJ....156..217N |
| 16570570-0420559 | 0.24 | 0.014 | -4.3071 | 0.0014 | 12.25 | 5.130 | 1.212 | 2012AcA....62...67K |
| 02004725-1021209 | 0.34 | 0.188 | -4.7907 | 0.0026 | 14.118 | 5.026 | 14.793 | 2018AJ....156..217N |
| 18494929-2350101 | 0.18 | 0.034 | -4.5243 | 0.0015 | 10.5 | 5.130 | 2.869 | 2007AcA....57..149K |
| 20035892-0807472 | 0.33 | 0.946 | -5.6530 | 0.0077 | 13.54 | 5.254 | 84.991 | 2018AJ....156..217N |
| 21390081-2409280 | 0.21 | 1.152 | -6.1949 | 0.0190 | 13.45 | 5.091 | 94.254 | 2018AJ....156..217N |
| 23071524-2307533 | 0.30 | 0.720 | -5.2780 | 0.0077 | 13.587 | 4.849 | 51.204 | 2018AJ....156..217N |
| 00094508-4201396 | 0.30 | 0.009 | -4.3392 | 0.0018 | 13.62 | 5.397 | 0.859 | 2018AJ....156..217N |
| 00310412-7201061 | 0.31 | 0.906 | -5.3879 | 0.0074 | 13.69 | 5.245 | 80.969 | 2018AJ....156..217N |
| 01040695-6522272 | 0.17 | 0.006 | -4.4889 | 0.0024 | 13.98 | 5.448 | 0.624 | 2018AJ....156..217N |
| 02014384-1017295 | 0.19 | 0.034 | -4.5400 | 0.0022 | 14.473 | 5.284 | 3.152 | 2018AJ....156..217N |
| 03100305-2341308 | 0.40 | 0.028 | -4.2336 | 0.0017 | 13.502 | 4.935 | 2.083 | 2018AJ....156..217N |
| 03205178-6351524 | 0.33 | 1.029 | -5.6288 | 0.0096 | 13.433 | 5.238 | 91.622 | 2018AJ....156..217N |
| 07401183-4257406 | 0.15 | 0.002 | -4.3365 | 0.0022 | 13.81 | 6.042 | 0.307 | 2018AJ....156..217N |
| 08184619-4806172 | 0.37 | 0.021 | -4.2834 | 0.0025 | 14.37 | 5.019 | 1.653 | 2018AJ....156..217N |
| 08443891-4805218 | 0.20 | 1.348 | -5.6682 | 0.0067 | 13.932 | 5.370 | 129.513 | 2018AJ....156..217N |
| 09342791-2643267 | 0.19 | 0.007 | -4.3415 | 0.0025 | 13.992 | 5.373 | 0.694 | 2018AJ....156..217N |
| 09524176-1536137 | 0.26 | 1.342 | -5.6319 | 0.0110 | 13.43 | 4.923 | 99.662 | 2018AJ....156..217N |
| 11075025-3421003 | 0.25 | 0.068 | -4.2250 | 0.0032 | 15.04 | 5.633 | 7.611 | 2018AJ....156..217N |
| 11575352-2349007 | 0.39 | 0.031 | -4.2952 | 0.0026 | 14.77 | 5.415 | 3.067 | 2018AJ....156..217N |
| 12102834-1310234 | 0.36 | 0.435 | -4.6892 | 0.0029 | 13.83 | 5.418 | 42.985 | 2018AJ....156..217N |
| 12440075-1110302 | 0.18 | 0.020 | -4.4053 | 0.0033 | 14.22 | 5.546 | 2.099 | 2018AJ....156..217N |
| 13442092-2618350 | 0.35 | 2.032 | -5.9634 | 0.0253 | 13.253 | 4.968 | 154.885 | 2018AJ....156..217N |
| 14253413-1148515 | 0.51 | 0.301 | -4.7641 | 0.0030 | 13.512 | 5.121 | 25.012 | 2018AJ....156..217N |
| 14340491-1824106 | 0.38 | 0.271 | -4.6093 | 0.0038 | 14.346 | 5.638 | 30.396 | 2018AJ....156..217N |
| 15154371-0725208 | 0.38 | 0.050 | -4.6214 | 0.0023 | 12.93 | 5.224 | 4.379 | 2018AJ....156..217N |
| 15290145-0612461 | 0.46 | 0.095 | -4.2015 | 0.0017 | 14.011 | 5.230 | 8.434 | 2018AJ....156..217N |
| 16204186-2005139 | 0.45 | 0.031 | -4.3900 | 0.0035 | 13.68 | 5.261 | 2.814 | 2018AJ....156..217N |
| 16475517-6509116 | 0.17 | 0.889 | -4.8744 | 0.0045 | 13.98 | 5.101 | 73.142 | 2018AJ....156..217N |
| 20091824-0113377 | 0.15 | 0.010 | -4.3772 | 0.0023 | 14.47 | 5.958 | 1.374 | 2018AJ....156..217N |
| 20273733-5452592 | 0.35 | 1.520 | -5.9982 | 0.0181 | 13.18 | 5.259 | 136.924 | 2018AJ....156..217N |
| 20444800-1453208 | 0.49 | 0.073 | -4.4912 | 0.0023 | 14.445 | 5.305 | 6.715 | 2018AJ....156..217N |
| 15404341-5101357 | 0.10 | 0.318 | -5.0062 | 0.0081 | 15.26 | 7.317 | 93.702 | 2018AJ....156..217N |
| 22480446-2422075 | 0.20 | 0.005 | -4.4123 | 0.0016 | 12.59 | 5.384 | 0.466 | 2013AJ....146..154M |
| 06393742-2101333 | 0.26 | 0.952 | -5.2524 | 0.0069 | 12.77 | 5.120 | 79.152 | 2018AJ....156..217N |
| 04130560+1514520 | 0.30 | 0.019 | -4.4775 | 0.0088 | 15.881 | 5.437 | 1.881 | 2016ApJ...818..46M |
| 02411510-0432177 | 0.20 | 0.004 | -4.4272 | 0.0016 | 13.79 | 5.544 | 0.400 | 2020ApJ...905..107M |
| 11381671-7721484 | 0.12 | 0.958 | -5.5015 | 0.0369 | 14.78 | 6.259 | 153.506 | This Work |
| 12384914-3822527 | 0.15 | 2.527 | -6.0690 | 0.0156 | 12.75 | 5.364 | 241.913 | This Work |
| 13464102-5830117 | 0.48 | 1.340 | -5.6977 | 0.0146 | | | 65.017 | This Work |
| 15165576-0037116 | 0.31 | 0.157 | -4.0704 | 0.0024 | 14.469 | 5.364 | 15.028 | This Work |
| 19204795-4533283 | 0.18 | 1.706 | -5.8392 | 0.0091 | 12.25 | 5.405 | 167.225 | This Work |
| 21362532-4401005 | 0.20 | 1.886 | -5.8978 | 0.0168 | 14.14 | 5.610 | 207.983 | This Work |

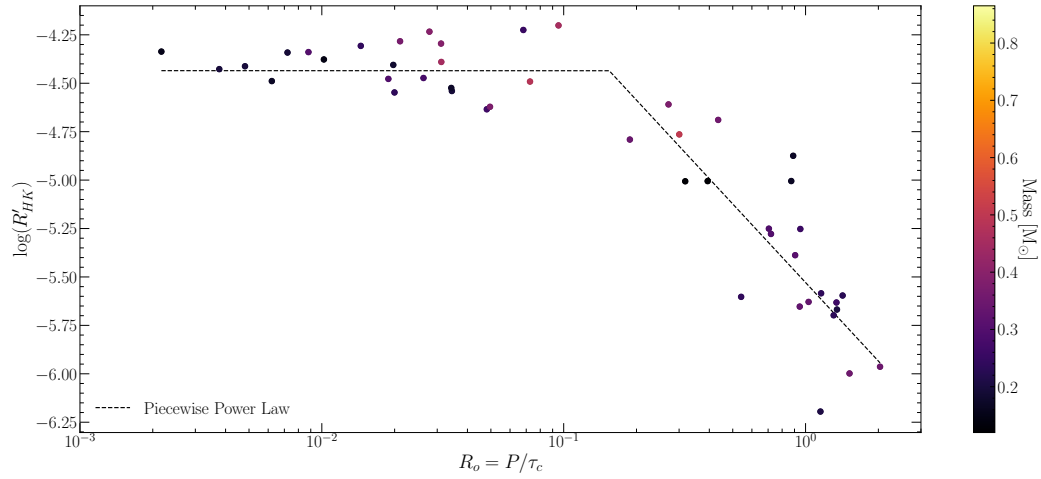


Figure 3.2: Rotation activity relation from this work. The color axis gives each stars mass. The dashed line is the best fit to our data set.

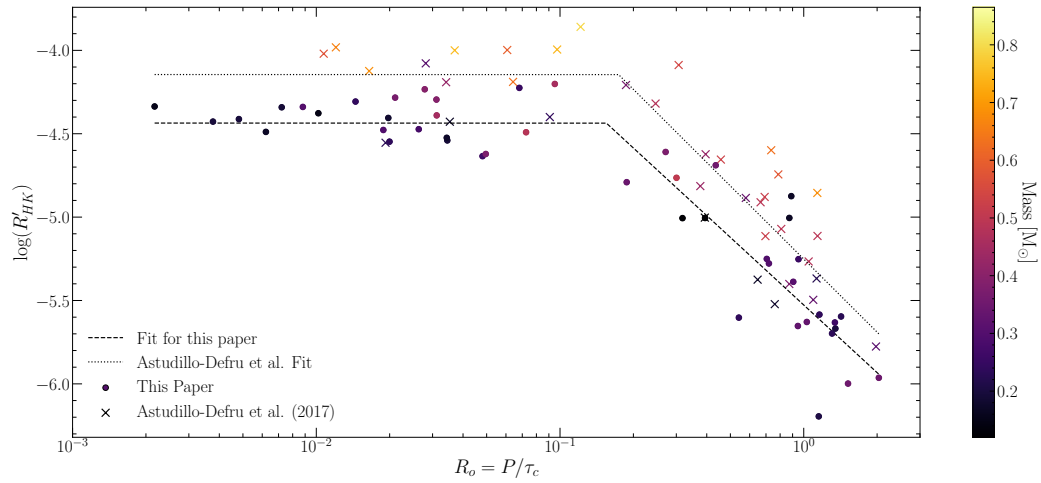


Figure 3.3: Rotation activity relation for both our work and ?. The dotted line is the best fit to the re-derived rotation-activity relation from ?. Note that targets from ? are systematically higher than targets presented here as a consequence of the range in mass probed by the samples.

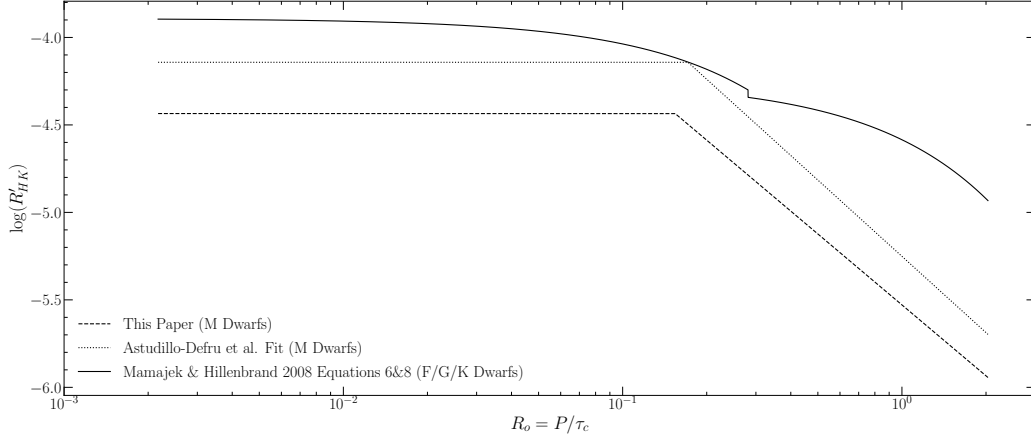


Figure 3.4: Derived rotation-activity curves from this work, ? and ?. Note both that ? focuses their work on earlier spectral classes and fits the rotation activity relation in linear space.

- $Ro_s = 0.155 \pm 0.045$
- $\log(R_s) = -4.436 \pm 0.048$

A comparison of the rotation activity derived in this work to those from both ? and ? is presented in Figure 3.4. For the 6 targets which do not have measured rotational periods we include an estimate of Ro and p_{rot} in the machine readable version of Table 3.1. The convective overturn timescale for one of these 6 targets (2MASS J13464102-5830117) can not be inferred via Equation 3.8 as it lacks a V-K color measurement. Instead, we infer τ_c via ? Equation 6 (this paper Equation 3.10) using mass. Similar to our manner of inferring τ_c via color, when inferring τ_c via mass, we adopt the larger of the two antisymmetric errors from ?.

$$\log_{10}(\tau_c) = 2.33 \pm 0.06 - 1.5 \pm 0.21 (M/M_\odot) + 0.31 \pm 0.17 (M/M_\odot)^2 \quad (3.10)$$

Note that R'_HK for one of six of these targets (2MASS J15165576-0037116) is consistent to within 1σ of the saturated value; therefore, the reported Ro for this target should only be taken as an upper bound. The remaining five targets have measured R'_HK values consistent with the unsat-

urated regime. Estimated periods are consistent with previous constraints. Of the six stars, two were listed as non-detections in ?, and the remaining four as uncertain (possible) detections. Of the four classed as uncertain, 2MASS 12384914-3822527 and 2MASS 19204795-4533283 have candidate periods > 100 days and non-detections of H-alpha emission (?). These two stars and the two non-detections have Ca II H&K activity levels suggesting very long periods. 2MASS 13464102-5830117 has a candidate period of 45 days, and 2MASS 15165576-0037116 of 0.8 days, both consistent with their higher levels of Ca II H&K emission.

As a test of the proposed weak correlation between activity and rotation in the “saturated” regime seen in some works (????) — though not in others (???) — we fit a second model whose power law index is allowed to vary at $Ro < Ro_s$. We find a saturated regime power law index of -0.052 ± 0.117 , consistent with 0 to within 1σ . Moreover, all other parameter for this model are consistent to within one σ of the nominal parameters for the model where the index is constrained to 0 below $Ro = Ro_s$. We can constrain the slope in the saturated regime to be between -0.363 and 0.259 at the 3σ confidence level. Ultimately, we adopt the most standard activity interpretation, a fully-saturated regime at $Ro < Ro_s$.

We investigate whether our lack of detection of a slope for $Ro < Ro_s$ is due to the limited number of observations in that region when compared to other works (e.g. ?, 93 targets $Ro < Ro_s$) through injection and recovery tests. We inject, fake, rotation-activity measurements into the saturated regime with an a priori slope of -0.13 — the same as in ?. These fake data are given a standard deviation equal to the standard deviation of our residuals (12%). We perform the same MCMC model fitting to this new data set as was done with the original dataset multiple times, each with progressively more injected data, until we can detect the injected slope to the three sigma confidence level. Ultimately, we need more than 65 data points — 43 more than we observed in the saturated regime — to

consistently recover this slope. Therefore, given the spread of our data we cannot detect slopes on the order of what has previously been reported in the literature.

We observe a gap in rotational period **over a comparable range** to the one presented in ? Figure 2. Namely, that M-dwarfs are preferentially observed as either fast or slow rotators, with a seeming lack of stars existing at mid rotational periods. This period gap manifests in the Rossby Number and can be seen in Figure 3.3 as a lack of our targets near to the knee-point in the fit. **This period gap likely corresponds to that seen by ?, who found a paucity of M dwarfs at intermediate activity levels in Ca II H&K and note the similarity to the Vaughn-Preston gap established in higher mass stars (?).** ? also identify a double-gap in x-ray activity for stars in the unsaturated regime; it is not clear that the gap **we see is related.** As a consequence of this period gap, there exists a degeneracy in our data between moving the knee-point and allowing the activity level to vary in the saturated regime. In the following, we adopt the model of a fully saturated regime.

We wish to compare our best fit parameters to those derived in ?; however, the authors of that paper do not fit the knee-point of the rotation-activity relation. They select the canonical value for the rotational period separating the saturated regime from the unsaturated regime ($P_{rot,s} = 10$ days) and use a fixed convective overturn timescale ($\tau_c = 70$ days). To make our comparison more meaningful we use the P_{rot} and $V - K$ colors presented in ? to re-derive Ro values using τ_c (?). Doing this for all targets presented in ? Table 3 and fitting the same piecewise power law as before, we find best fit parameters of $Ro_s = 0.17 \pm 0.04$, $\log(R_s) = -4.140 \pm 0.067$, and $k = -1.43 \pm 0.21$. Compared to the best fit parameters for our data, Ro_s and the unsaturated regime's index, k , are consistent to within one sigma, while the saturated value, R_s , differs.

The mass ranges of our respective samples explain the differences in saturation values between our work and that of ?. Our work focuses on mid-to-late M-dwarfs and includes no stars above a mass of $0.5 M_\odot$ (Figure 3.5). **The strength of Ca II H&K emission is known to decrease as stellar mass decreases (???).** As ?

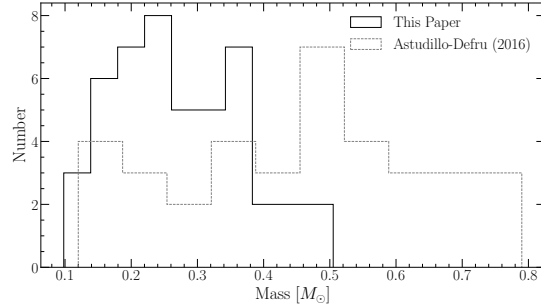


Figure 3.5: Distribution of masses between our sample and the sample presented in ?. Note how the two studies have approximately the same sample sizes; however, our sample is more tightly concentrated at lower masses \later spectral classes.

note, this is the opposite as the trend seen in H-alpha; the latter primarily reflects the increasing length of time that lower M dwarfs remain active and rapidly rotating (??).

A mass dependence can be seen in Figure 10 in ?, consistent with expectations from the literature. If we clip the data from ? Table 3 to the same mass range as our data-set ($M_* < 0.5M_{\odot}$) and fit the same function as above, we find that all best fit parameters are consistent to within one sigma between the two data-sets.

We also compare our best fit R_{obs} to both those derived in ? using H_{α} as an activity measure and those derived in (??) using L_X/L_{bol} as an activity measure. Works using L_X/L_{bol} identify a similar, yet not consistent to within one sigma result for R_{obs} ; while, the value of k we find here is consistent between all four works. Therefore, we find similar results not only to other work using the same activity tracer, but also a power-law slope that is consistent with work using different tracers.

3.5 Magnetic Activities in M dwarfs Closing Thoughts

In this work we have approximately doubled the number of M-dwarfs with both empirically measured R'_{HK} with $M_* < 0.5M_{\odot}$. This has enabled us to more precisely constrain the rotation-activity relation. This relationship is consistent with other measurements using R'_{HK} , and L_X/L_{bol} ; our data does not require a slope in the saturated regime. Finally, we identify a mass dependence in the activity level of

the saturated regime, consistent with trends seen in more massive stars in previous works.

Chapter 4

Jao Gap

4.1 Jao Gap Sensitivity to Opacity

4.2 INTRODUCTION

Due to the initial mass requirements of the molecular clouds which collapse to form stars, star formation is strongly biased towards lower mass, later spectral class stars when compared to higher mass stars. Partly as a result of this bias and partly as a result of their extremely long main-sequence lifetimes, M Dwarfs make up approximately 70 percent of all stars in the galaxy. Moreover, some planet search campaigns have focused on M Dwarfs due to the relative ease of detecting small planets in their habitable zones (e.g. ?). M Dwarfs then represent both a key component of the galactic stellar population as well as the possible set of stars which may host habitable exoplanets. Given this key location M Dwarfs occupy in modern astronomy it is important to have a thorough understanding of their structure and evolution.

? discovered a novel feature in the Gaia Data Release 2 (DR2) $G_{BP} - G_{RP}$ color-magnitude-diagram. Around $M_G = 10$ there is an approximately 17 percent decrease in stellar density of the sample of stars ? considered. Subsequently, this has become known as either the Jao Gap, or Gaia M Dwarf Gap. Following the initial detection of the Gap in DR2 the Gap has also potentially been observed in 2MASS (??); however, the significance of this detection is quite weak and it relies on the prior of the Gap's location from Gaia data. Further, the Gap is also present in Gaia Early Data Release

3 (EDR3) (?). These EDR3 and 2MASS data sets then indicate that this feature is not a bias inherent to DR2.

The Gap is generally attributed to convective instabilities in the cores of stars straddling the fully convective transition mass ($0.3 - 0.35 M_{\odot}$) (?). These instabilities interrupt the normal, slow, main sequence luminosity evolution of a star and result in luminosities lower than expected from the main sequence mass-luminosity relation (?).

The Jao Gap, inherently a feature of M Dwarf populations, provides an enticing and unique view into the interior physics of these stars (?). This is especially important as, unlike more massive stars, M Dwarf seismology is infeasible due to the short periods and extremely small magnitudes which both radial and low-order low-degree non-radial seismic waves are predicted to have in such low mass stars (?). The Jao Gap therefore provides one of the only current methods to probe the interior physics of M Dwarfs.

Despite the early success of modeling the Gap some issues remain. ?? identify that the Gap has a wedge shape which has not been successful reproduced by any current modeling efforts and which implies a somewhat unusual population composition of young, metal-poor stars. Further, ? identify substructure, an additional over density of stars, directly below the Gap, again a feature not yet fully captured by current models.

All currently published models of the Jao Gap make use of OPAL high temperature radiative opacities. Here we investigate the effect of using the more up-to-date OPLIB high temperature radiative opacities and whether these opacity tables bring models more in line with observations. In Section 4.3 we provide an overview of the physics believed to result in the Jao Gap, in Section 4.4 we review the differences between OPAL and OPLIB and describe how we update DSEP to use OPLIB opacity tables. Section 4.7 walks through the stellar evolution and population synthesis modeling we perform. Finally, in Section 4.8 we present our findings.

4.3 Jao Gap

A theoretical explanation for the Jao Gap (Figure 4.1) comes from ?, who propose that in a star directly above the transition mass, due to asymmetric production and destruction of ${}^3\text{He}$ during the proton-proton I chain (ppI), periodic luminosity variations can be induced. This process is known as convective-kissing instability. Very shortly after the zero-age main sequence such a star will briefly develop a radiative core; however, as the core temperature exceeds 7×10^6 K, enough energy will be produced by the ppI chain that the core once again becomes convective. At this point the star exists with both a convective core and envelope, in addition to a thin, radiative layer separating the two. Subsequently, asymmetries in ppI affect the evolution of the star's convective core.

While kissing instability has been the most widely adopted model to explain the existence of the Jao Gap, slightly different mechanisms have also been proposed. ? make use of a fully implicit stellar evolution suite which treats convective mixing as a diffusive property. ? treat convective mixing this way in order to account for a core deuterium concentration gradient proposed by ?. Under this treatment the instability results only in a single mixing event — as opposed to periodic mixing events. Single mixing events may be more in line with observations (see section 4.8 for more details on how periodic mixings can effect a synthetic population) where there is only well documented evidence of a single gap. However, recent work by ? which identify an second under density of stars below the canonical gap, does leave the door open for the periodic mixing events.

The proton-proton I chain constitutes three reactions

1. $p + p \longrightarrow d + e^+ + \nu_e$
2. $p + d \longrightarrow {}^3\text{He} + \gamma$
3. ${}^3\text{He} + {}^3\text{He} \longrightarrow {}^3\text{He} + 2p$

Initially, reaction 3 of ppI consumes ${}^3\text{He}$ at a slower rate than it is produced by reaction 2 and as a result, the core ${}^3\text{He}$ abundance and consequently the rate of reaction

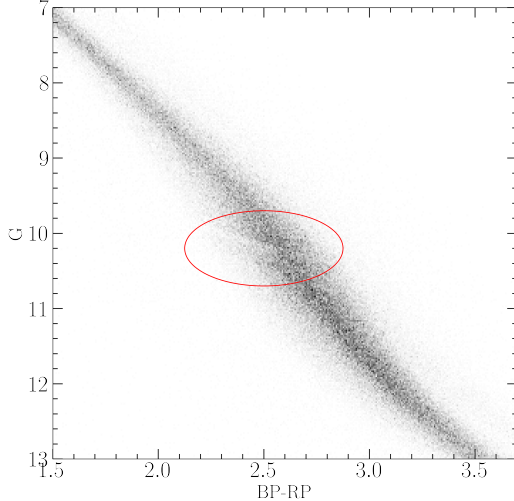


Figure 4.1: The Jao Gap (circled) seen in the Gaia Catalogue of Nearby Stars (?).

3, increases with time. The core convective zone expands as more of the star becomes unstable to convection. This expansion continues until the core connects with the convective envelope. At this point convective mixing can transport material throughout the entire star and the high concentration of ^3He rapidly diffuses outward, away from the core, decreasing energy generation as reaction 3 slows down. Ultimately, this leads to the convective region around the core pulling back away from the convective envelope, leaving in place the radiative transition zone, at which point ^3He concentrations grow in the core until it once again expands to meet the envelope. These periodic mixing events will continue until ^3He concentrations throughout the star reach an equilibrium ultimately resulting in a fully convective star. Figure 4.2 traces the evolution of a characteristic star within the Jao Gap’s mass range.

4.3.1 Efforts to Model the Gap

Since the identification of the Gap, stellar modeling has been conducted to better constrain its location, effects, and exact cause. Both ? and ? identify that the Gap’s mass location is correlated with model metallicity — the mass-luminosity discontinuity in lower metallicity models being at a commensurately lower mass. ? suggests this dependence is due to the steep relation of the radiative temperature gradient, ∇_{rad} , on temperature and, in turn, on stellar mass.

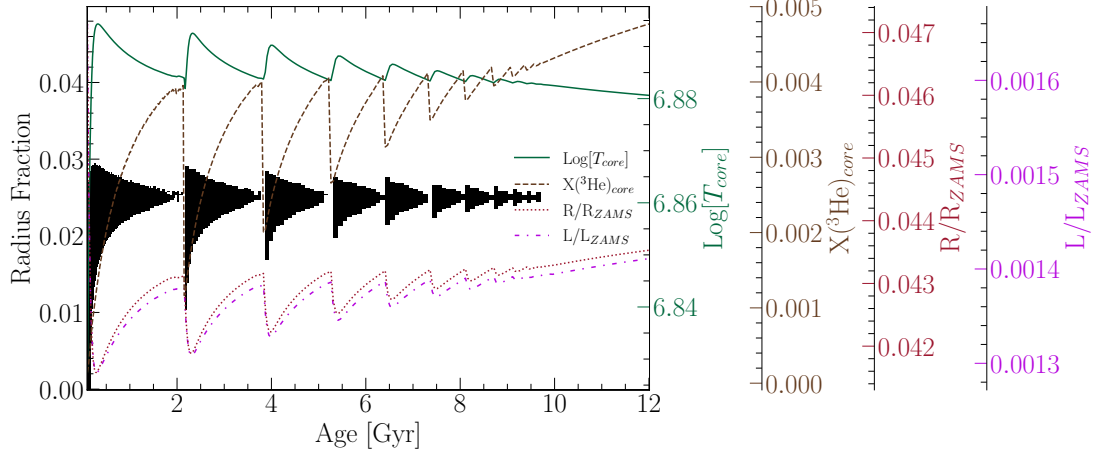


Figure 4.2: Diagram for a characteristic stellar model of $0.35625 M_{\odot}$ which is within the Jao Gap’s mass range. The black shaded regions denote whether, at a particular model age, a radial shell within the model is radiative (with white meaning convective). The lines trace the models core temperature, core ${}^3\text{He}$ mass fraction, fractional luminosity wrt. the zero age main sequence and fractional radius wrt. the zero age main sequence.

$$\nabla_{rad} \propto \frac{L\kappa}{T^4} \quad (4.1)$$

As metallicity decreases so does opacity, which, by Equation 4.1, dramatically lowers the temperature at which radiation will dominate energy transport (?). Since main sequence stars are virialized the core temperature is proportional to the core density and total mass. Therefore, if the core temperature where convective-kissing instability is expected decreases with metallicity, so too will the mass of stars which experience such instabilities.

The strong opacity dependence of the Jao Gap begs the question: what is the effect of different opacity calculations on Gap properties. As we can see above, changing opacity should affect the Gap’s location in the mass-luminosity relation and therefore in a color-magnitude diagram (?) with an approximate 0.16 G-magnitude difference between the observed and modeled Gaps. Opacity provides one, as yet unexplored, parameter which has the potential to resolve these discrepancies.

4.4 Updated Opacities

Multiple groups have released high-temperature opacities including, the Opacity Project (OP ?), Laurence Livermore National Labs OPAL opacity tables (?), and Los Alamos National Labs OPLIB opacity tables (?). OPAL high-temperature radiative opacity tables in particular are very widely used by current generation isochrone grids (e.g. Dartmouth, MIST, & StarEvol, ???). OPLIB opacity tables (?) are not widely used but include the most up-to-date plasma modeling.

While the overall effect on the CMD of using OPLIB compared to OPAL tables is small, the strong theoretical opacity dependence of the Jao Gap raises the potential for these small effects to measurably shift the Gap's location. We update DSEP to use high temperature opacity tables based on measurements from Los Alamos national Labs T-1 group (OPLIB, ?). The OPLIB tables are created with ATOMIC (???), a modern LTE and non-LTE opacity and plasma modeling code. These updated tables were initially created in order to incorporate the most up to date plasma physics at the time (?).

OPLIB tables include monochromatic Rosseland mean opacities — composed from bound-bound, bound-free, free-free, and scattering opacities — for elements hydrogen through zinc over temperatures 0.5eV to 100 keV ($5802\text{ K} - 1.16 \times 10^9\text{ K}$) and for mass densities from approximately 10^{-8} g cm^{-3} up to approximately 10^4 g cm^{-3} (though the exact mass density range varies as a function of temperature).

DSEP ramps the ? low temperature opacities to high temperature opacities tables between $10^{4.3}\text{ K}$ and $10^{4.5}\text{ K}$; therefore, only differences between high-temperature opacity sources above $10^{4.3}\text{ K}$ can effect model evolution. When comparing OPAL and OPLIB opacity tables (Figure 4.3) we find OPLIB opacities are systematically lower than OPAL opacities for temperatures above 10^5 K . Between $10^{4.3}$ and 10^5 K OPLIB opacities are larger than OPAL opacities. These generally lower opacities will decrease the radiative temperature gradient throughout much of the radius of a model.

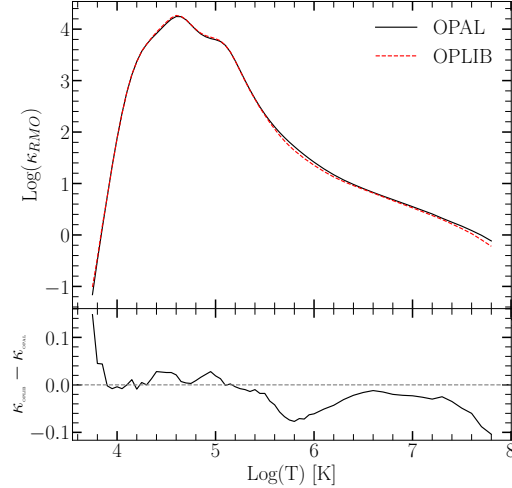


Figure 4.3: Rosseland mean opacity with the GS98 solar composition for both OPAL opacities and OPLIB opacities (top). Residuals between OPLIB opacities and OPAL opacities (bottom). These opacities are plotted at $\log_{10}(R) = -0.5$, $X = 0.7$, and $Z = 0.02$. $\log_{10}(R) = -0.5$ approximates much of the interior a $0.35 M_\odot$ model. Note how the OPLIB opacities are systematically lower than the OPAL opacities for temperatures above $10^{5.2}$ K.

4.4.1 Table Querying and Conversion

The high-temperature opacity tables used by DSEP and most other stellar evolution programs give Rosseland-mean opacity, κ_R , along three dimensions: temperature, a density proxy R (Equation 4.2; $T_6 = T \times 10^{-6}$, ρ is the mass density), and composition.

$$R = \frac{\rho}{T_6^3} \quad (4.2)$$

OPLIB tables may be queried from a web interface¹; however, OPLIB opacities are parametrized using mass-density and temperature instead of R and temperature. It is most efficient for us to convert these tables to the OPAL format instead of modifying DSEP to use the OPLIB format directly. In order to generate many tables easily and quickly we develop a web scraper (`pyTOPSScrape`, ?) which can automatically retrieve all the tables needed to build an opacity table in the OPAL format. `pyTOPSScrape`² has been released under the permissive MIT license with the consent of the Los Alamos

¹<https://aphysics2.lanl.gov/apps/>

²<https://github.com/tboudreaux/pytopsscrape>

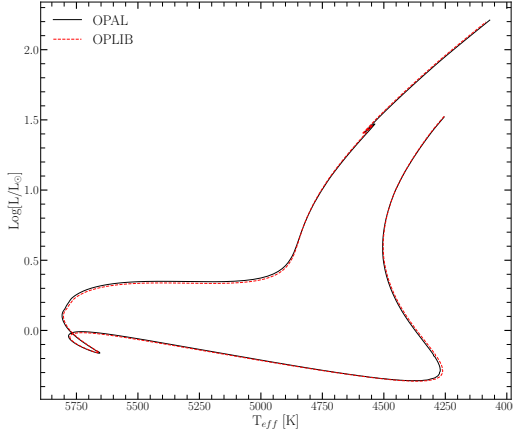


Figure 4.4: HR Diagram for the two SCSMs, OPAL and OPLIB. OPLIB is shown as a red dashed line.

T-1 group. For a detailed discussion of how the web scraper works and how OPLIB tables are transformed into a format DSEP can use see Appendices 4.5 & 4.6.

4.4.2 Solar Calibrated Stellar Models

In order to validate the OPLIB opacities, we generate a solar calibrated stellar model (SCSM) using these new tables. We first manually calibrate the surface Z/X abundance to within one part in 100 of the solar value (? , Z/X=0.23). Subsequently, we allow both the convective mixing length parameter, α_{ML} , and the initial Hydrogen mass fraction, X , to vary simultaneously, minimizing the difference, to within one part in 10^5 , between resultant models' final radius and luminosity to those of the sun. Finally, we confirm that the model's surface Z/X abundance is still within one part in 100 of the solar value.

Solar calibrated stellar models evolved using GS98 OPAL and OPLIB opacity tables (Figure 4.4) differ $\sim 0.5\%$ in the SCSM hydrogen mass fractions and $\sim 1.5\%$ in the SCSM convective mixing length parameters (Table 4.1). While the two evolutionary tracks are very similar, note that the OPLIB SCSM's luminosity is systematically lower past the solar age. While at the solar age the OPLIB SCSM luminosity is effectively the same as the OPAL SCSM. This luminosity difference between OPAL and OPLIB based models is not inconsistent with expectations given the more shallow radiative temperature gradient resulting from the lower OPLIB opacities

| Model | X | α_{ML} |
|-------|--------|---------------|
| OPAL | 0.7066 | 1.9333 |
| OPLIB | 0.7107 | 1.9629 |

Table 4.1: Optimized parameters for SCSMs evolved using OPAL and OPLIB high temperature opacity tables.

4.5 pyTOPSScrape

`pyTOPSScrape` provides an easy to use command line and python interface for the OPLIB opacity tables accessed through the TOPS web form. Extensive documentation of both the command line and programmatic interfaces is linked in the version controlled repository. However, here we provide a brief, illustrative, example of potential use.

Assuming `pyTOPSScrape` has been installed and given some working directory which contains a file describing a base composition (“comp.dat”) and another file containing a list of rescalings of that base composition (“rescalings.dat”) (both of these file formats are described in detail in the documentation), one can query OPLIB opacity tables and convert them to a form mimicking that of type 1 OPAL high temperature opacity tables using the following shell command.

```
$ generateTOPStables comp.dat rescalings.dat -d ./TOPSCache -o out.opac -j 20
```

For further examples of `pyTOPSScrape` please visit the repository.

4.6 Interpolating $\rho \rightarrow \mathbf{R}$

OPLIB parameterizes κ_R as a function of mass density, temperature in keV, and composition. Type 1 OPAL high temperature opacity tables, which DSEP and many other stellar evolution programs use, instead parameterizes opacity as a function of temperature in Kelvin, R (Equation 4.3), and composition. The conversion from temperature in keV to Kelvin is trivial (Equation 4.4).

$$R = \frac{\rho}{T_6^3} \quad (4.3)$$

$$T_K = T_{keV} * 11604525.0061657 \quad (4.4)$$

However, the conversion from mass density to R is more involved. Because R is coupled with both mass density and temperature there is no way to directly convert tabulated values of opacity reported in the OPLIB tables to their equivalents in R space. The TOPS webform does allow for a density range to be specified at a specific temperature, which allows for R values to be directly specified. However, issuing a query to the TOPS webform for not just every composition in a Type 1 OPAL high temperature opacity table but also every temperature for every composition will increase the number of calls to the webform by a factor of 70. Therefore, instead of directly specifying R through the density range we choose to query tables over a broad temperature and density range and then rotate these tables, interpolating $\kappa_R(\rho, T_{eff}) \rightarrow \kappa_R(R, T_{eff})$.

To perform this rotation we use the `interp2d` function within `scipy`'s `interpolate` (?) module to construct a cubic bivariate B-spline (?) interpolating function s , with a smoothing factor of 0, representing the surface $\kappa_R(\rho, T_{eff})$. For each R^i and T_{eff}^j reported in type 1 OPAL tables, we evaluate Equation 4.3 to find $\rho^{ij} = \rho(T_{eff}^j, R^i)$. Opacities in T_{eff} , R space are then inferred as $\kappa_R^{ij}(R^i, T_{eff}^j) = s(\rho^{ij}, T_{eff}^j)$.

As first-order validation of this interpolation scheme we can perform a similar interpolation in the opposite direction, rotating the tables back to $\kappa_R(\rho, T_{eff})$ and then comparing the initial, “raw”, opacities to those which have gone through the interpolations process. Figure 4.5 shows the fractional difference between the raw opacities and a set which have gone through this double interpolation. The red line denotes $\log(R) = -0.79$ where models near the Jao Gap mass range will tend to sit for much of their radius. Along the $\log(R) = -0.79$ line the mean fractional difference is $\langle \delta \rangle = 0.005$ with an uncertainty of $\sigma_{\langle \delta \rangle} = 0.013$. One point of note is that, because the initial rotation into $\log(R)$ space also reduces the domain of the opacity function, interpolation-edge effects which we avoid initially by extending the domain past what type 1 OPAL tables include cannot be avoided when interpolating back into ρ space.

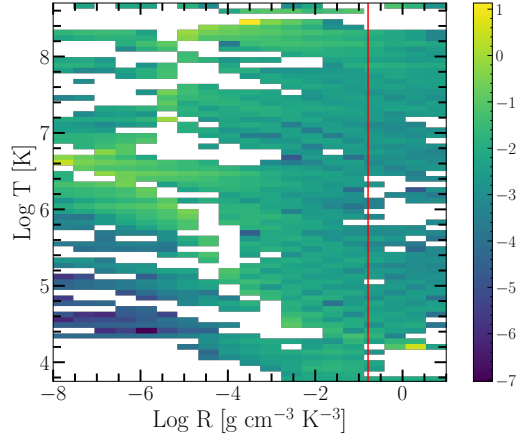


Figure 4.5: Log Fractional Difference between opacities in $\kappa_R(\rho, T_{eff})$ space directly queried from the OPLIB web-form and those which have been interpolated into $\log(R)$ space and back. Note that, due to the temperature grid of type 1 OPAL tables not aligning perfectly with the temperature grid OPLIB uses there may be edge effects where the interpolation is poorly constrained. The red line corresponds to $\log(R) = -0.79$ where much of a stellar model's radius exists.

4.7 Modeling

In order to model the Jao Gap we evolve two extremely finely sampled mass grids of models. One of these grids uses the OPAL high-temperature opacity tables while the other uses the OPLIB tables (Figure 4.6). Each grid evolves a model every $0.00025 M_\odot$ from 0.2 to $0.4 M_\odot$ and every $0.005 M_\odot$ from 0.4 to $0.8 M_\odot$. All models in both grids use a GS98 solar composition, the (1, 101, 0) FreeEOS (version 2.7) configuration, and 1000 year old pre-main sequence polytropic models, with polytropic index 1.5, as their initial conditions. We include gravitational settling in our models where elements are grouped together. Finally, we set a maximum allowed timestep of 50 million years to assure that we fully resolve the build of core ^3He in gap stars.

Despite the alternative view of convection provided by ? discussed in Section 4.3, given that the mixing timescales in these low mass stars are so short (between 10^7 s and 10^8 s per ?, Figure 2 & Equation 39, which present the averaged velocity over the convection zone) instantaneous mixing is a valid approximation. Moreover, one principal motivation for a diffusive model of convective mixing has been to account for a deuterium concentration gradient which ? identify will develop when the deuterium

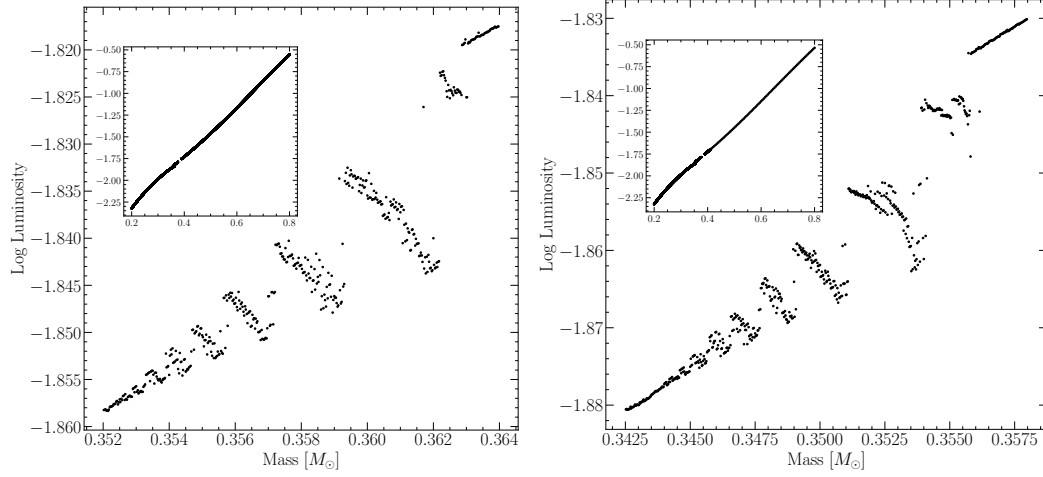


Figure 4.6: Mass-luminosity relation at 7 Gyrs for models evolved using OPAL opacity tables (top) and those evolved using OPLIB opacity tables (bottom). Note the lower mass range of the OPLIB Gap.

lifetime against proton capture is significantly shorter than the mixing timescale. However, the treatment of energy generation used by DSEP (?) avoids this issue by computing both the equilibrium deuterium abundance and luminosity of each shell individually, implicitly accounting for the overall luminosity discrepancy identified by ?.

Because in this work we are just interested in the location shift of the Gap as the opacity source varies, we do not model variations in composition. ??? all look at the effect composition has on Jao Gap location. They find that as population metallicity increases so too does the mass range and consequently the magnitude of the Gap. From an extremely low metallicity population ($Z=0.001$) to a population with a more solar like metallicity this shift in mass range can be up to $0.05 M_{\odot}$ (?).

4.7.1 Population Synthesis

In order to compare the Gap to observations we use in house population synthesis code. We empirically calibrate the relation between G, BP, and RP magnitudes and their uncertainties along with the parallax/G magnitude uncertainty relation using the Gaia Catalogue of Nearby Stars (GCNS, ?) and Equations 4.5 & 4.6. M_g is the Gaia G magnitude while M_i is the magnitude in the i^{th} band, G, BP, or RP. The

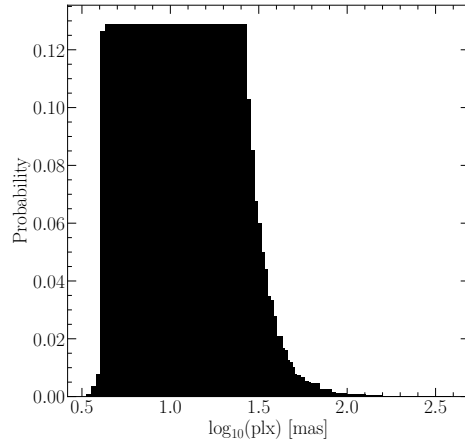


Figure 4.7: Probability distribution sampled when assigning true parallaxes to synthetic stars. This distribution is built from the GCNS and includes all stars with BP-RP colors between 2.3 and 2.9, the same color range of the Jao Gap.

coefficients a , b , and c determined using a non-linear least squares fitting routine. Equation 4.5 then models the relation between G magnitude and parallax uncertainty while Equation 4.6 models the relation between each magnitude and its uncertainty.

$$\sigma_{\text{plx}}(M_g) = ae^{bM_g} + c \quad (4.5)$$

$$\sigma_i(M_i) = ae^{M_i - b} + c \quad (4.6)$$

The full series of steps in our population synthesis code are:

1. Sample from a ? ($0.25M_\odot < M < 1M_\odot$, $\alpha = -1.34 \pm 0.07$) IMF to determine synthetic star mass.
2. Find the closest model above and below the synthetic star, linearly interpolate these models' T_{eff} , $\log(g)$, and $\log(L)$ to those at the synthetic star mass.
3. Convert synthetic star g , T_{eff} , and $\log(L)$ to Gaia G, BP, and RP magnitudes using the Gaia (E)DR3 bolometric corrections (?) along with code obtained thorough personal communication with Aaron Dotter (?).

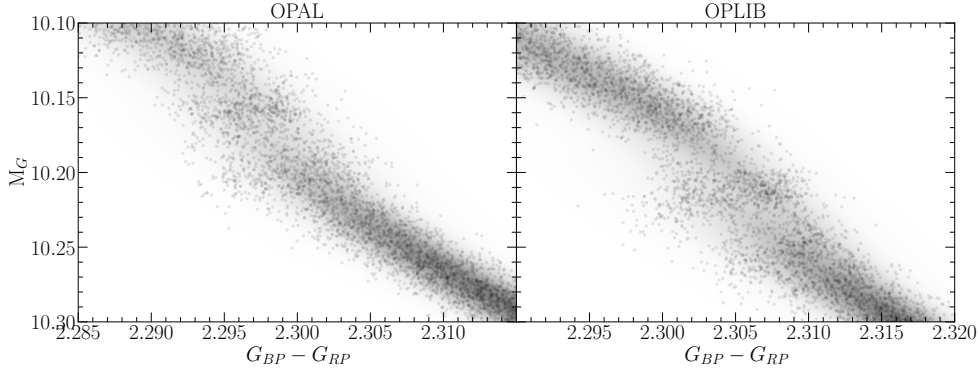


Figure 4.8: Population synthesis results for models evolved with OPAL (left) and models evolved with OPLIB (right). A Gaussian kernel-density estimate has been overlaid to better highlight the density variations.

4. Sample from the GCNS parallax distribution (Figure 4.7), limited to stars within the BP-RP color range of 2.3 – 2.9, to assign synthetic star a “true” parallax.
5. Use the true parallax to find an apparent magnitude for each filter.
6. Evaluate the empirical calibration given in Equation 4.5 to find an associated parallax uncertainty. Then sample from a normal distribution with a standard deviation equal to that uncertainty to adjust the true parallax resulting in an “observed” parallax.
7. Use the “observed” parallax and the apparent magnitude to find an “observed” magnitude.
8. Fit the empirical calibration given in Equation 4.6 to the GCNS and evaluate it to give a magnitude uncertainty scale in each band.
9. Adjust each magnitude by an amount sampled from a normal distribution with a standard deviation of the magnitude uncertainty scale found in the previous step.

This method then incorporates both photometric and astrometric uncertainties into our population synthesis. An example 7 Gyr old synthetic populations using OPAL and OPLIB opacities are presented in Figure 4.8.

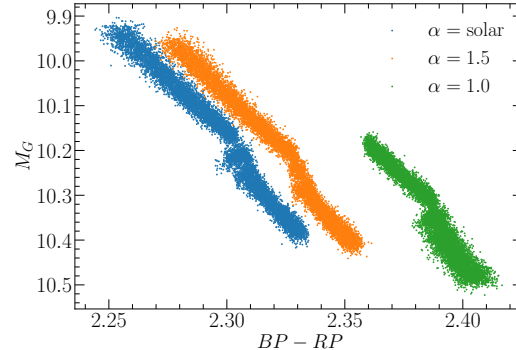


Figure 4.9: CMD showing OPLIB populations (from left to right) A, B, and C.

4.7.2 Mixing Length Dependence

In order to test the sensitivity of Gap properties to mixing length we evolve three separate sets OPLIB of models. The first uses a GS98 solar calibrated mixing length, the second uses a mixing length of 1.5, and the third uses a mixing length of 1.0.

We find a clear inverse correlation between mixing length parameter used and the magnitude of the Jao Gap Figures 4.9 & 4.10 ($\mu_G \propto -1.5\alpha_{ML}$, where μ_G is the mean magnitude of the Gap). This is somewhat surprising given the long established view that the mixing length parameter is of little relevance in fully convective stars (?). We find an approximate 0.3 magnitude shift in both the color and magnitude comparing a solar calibrated mixing length to a mixing length of 1.5, despite only a 16K difference in effective temperature at 7Gyr between two 0.3 solar mass models. The slight temperature differences between these models are attributable to the steeper adiabatic temperature gradients just below the atmosphere in the solar calibrated mixing length model compared to the $\alpha_{ML} = 1.5$ model ($\nabla_{ad,solar} - \nabla_{ad,1.5} \approx 0.05$). Despite this relatively small temperature variance, the large magnitude difference is expected due to the extreme sensitivity of the bolometric corrections on effective temperature at these low temperatures. The mixing length then provides a free parameter which may be used to shift the gap location in order to better match observations without having a major impact on the effective temperature of models. Moreover, recent work indicates that using a solar calibrated mixing length is not appropriate for all stars (e.g. ??).

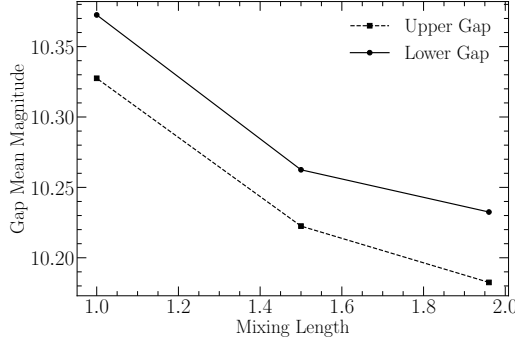


Figure 4.10: Location of the two identified paucities of stars in OPLIB synthetic populations as a function of the mixing length used.

Given the variability of gap location with mixing length, it is possible that a better fit to the gap location may be achieved through adjustment of the convective mixing length parameter. However, calibrations of the mixing length for stars other than the sun have focused on stars with effective temperature at or above that of the sun and there are no current calibrations of the mixing length parameter for M dwarfs. Moreover, there are additional uncertainties when comparing the predicted gap location to the measured gap location, such as those in the conversion from effective temperature, surface gravity, and luminosity to color, which must be considered if the mixing length is to be used as a gap location free parameter. Given the dangers of freely adjustable parameters and the lack of an a priori expectation for what the convective mixing parameter should be for the population of M Dwarfs in the Gaia DR2 and EDR3 CMD any attempt to use the Jao Gap magnitude to calibrate a mixing length value must be done with caution, and take into account the other uncertainties in the stellar models which could affect the Jao Gap magnitude.

4.8 Results

We quantify the Jao Gap location along the magnitude (Table 4.2) axis by sub-sampling our synthetic populations, finding the linear number density along the magnitude axis of each sub-sample, averaging these linear number densities, and extracting any peaks above a prominence threshold of 0.1 as potential magnitudes of the Jao Gap (Figure 4.11). Gap widths are measured at 50% the height of the peak promi-

| Model | Location | Prominence | Width |
|---------|----------|------------|-------|
| OPAL 1 | 10.138 | 0.593 | 0.027 |
| OPAL 2 | 10.183 | 0.529 | 0.023 |
| OPLIB 1 | 10.188 | 0.724 | 0.032 |
| OPLIB 2 | 10.233 | 0.386 | 0.027 |

Table 4.2: Locations identified as potential Gaps.

nence. We use the python package `scipy` (?) to both identify peaks and measure their widths.

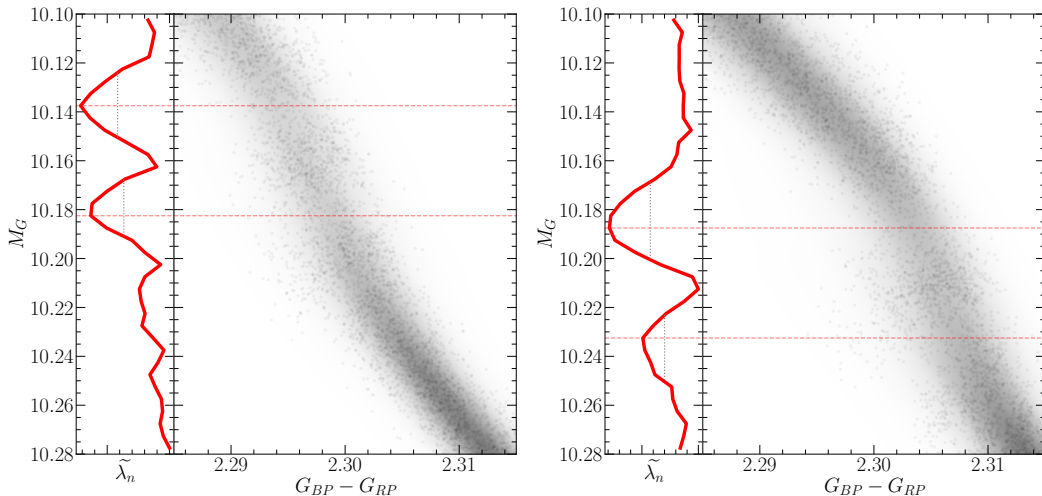


Figure 4.11: (right panels) OPAL (left) and OPLIB (right) synthetic populations. (left panels) Normalized linear number density along the magnitude axis. A dashed line has been extended from the peak through both panels to make clear where the identified Jao Gap location is wrt. to the population.

In both OPAL and OPLIB synthetic populations our Gap identification method finds two gaps above the prominence threshold. The identification of more than one gap is not inconsistent with the mass-luminosity relation seen in the grids we evolve. As noise is injected into a synthetic population smaller features will be smeared out while larger ones will tend to persist. The mass-luminosity relations shown in Figure 4.6 make it clear that there are: (1), multiple gaps due to stars of different masses undergoing convective mixing events at different ages, and (2), the gaps decrease in width moving to lower masses / redder. Therefore, the multiple gaps we identify are attributable to the two bluest gaps being wide enough to not smear out with noise. In fact, if we lower the prominence threshold just slightly from 0.1 to 0.09 we detect

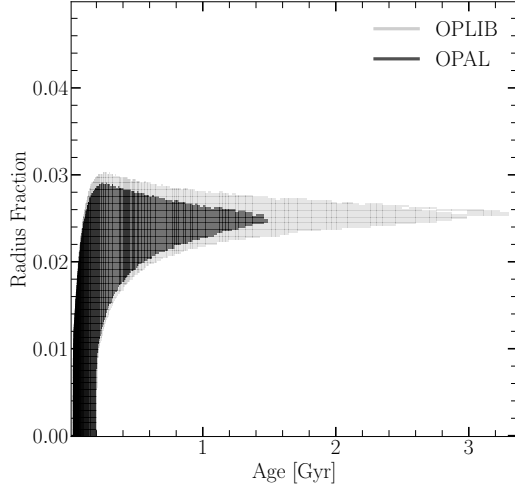


Figure 4.12: Portions of $0.3526 M_{\odot}$ OPAL and OPLIB stellar models showing the interior shells which are radiative (black region). Note that for clarity only one convective mixing event from each model is shown. Note how the radiative zone in the OPLIB model is larger.

a third gap in both the OPAL and OPLIB datasets where one would be expected.

Previous modeling efforts (e.g. ?) have not identified multiple gaps. This is likely due to two reasons: (1), previous studies have allowed metallicity to vary across their model grids, further smearing the gaps out, and (2), previous studies have used more coarse underlying mass grids, obscuring features smaller than their mass step. While this dual-gap structure has not been seen in models before, a more complex gap structure is not totally unprecedented as ? identifies an additional under-dense region below the primary gap in EDR3 data. As part of a follow up series of papers, we are conducting further work to incorporate metallicity variations while still using the finer mass sampling presented here.

The mean gap location of the OPLIB population is at a fainter magnitude than the mean gap location of the OPAL population. Consequently, in the OPLIB sample the convective mixing events which drive the kissing instability begin happening at lower masses (i.e. the convective transition mass decreases). A lower mass range will naturally result in a fainter mean gap magnitude.

Mixing events at lower masses in OPLIB models are attributable to the radially thicker, at the same mass, radiative zones (Figure 4.12). This thicker radiative zone

will take more time to break down and is characteristic of OPLIB models as of a result of their slightly lower opacities. A lower opacity fluid will have a more shallow radiative temperature gradient than a higher opacity fluid; however, as the adiabatic temperature gradient remains essentially unchanged as a function of radius, a larger interior radius of the model will remain unstable to radiation. This thicker radiative zone will increase the time it takes the core convective zone to meet up with convective envelope meaning that lower mass models can sustain a radiative zone for longer than they could otherwise; thus; lower opacities push the convective transition mass down. We can additionally see this longer lived radiative zone in the core ^3He mass fraction, in which OPLIB models reach much higher concentrations — at approximately the same growth rate — for the same mass as OPAL models do (Figure 4.13).

The most precise published Gap location comes from ? who use EDR3 to locate the Gap at $M_G \sim 10.3$, we identify the Gap at a similar location in the GCNS data. The Gap in populations evolved using OPLIB tables is closer to this measurement than it is in populations evolved using OPAL tables (Table 4.2). It should be noted that the exact location of the observed Gap is poorly captured by a single value as the Gap visibly compresses across the width of the main-sequence, wider on the blue edge and narrower on the red edge such that the observed Gap has downward facing a wedge shape (Figure 4.1). This wedge shape is not successfully reproduced by either any current models or the modeling we perform here. We elect then to specify the Gap location where this wedge is at its narrowest, on the red edge of the main sequence.

The Gaps identified in our modeling have widths of approximately 0.03 magnitudes, while the shift from OPAL to OPLIB opacities is 0.05 magnitudes. With the prior that the Gaps clearly shift before noise is injected we know that this shift is real. However, the shift magnitude and Gap width are of approximately the same size in our synthetic populations. Moreover, ? identify that the shift in the modeled Gap mass from $[\text{Fe}/\text{H}] = 0$ to $[\text{Fe}/\text{H}] = +0.5$ as $0.04M_\odot$, whereas we only see an approximate $0.01 M_\odot$ shift between OPAL and OPLIB models. Therefore, the Gap location will likely not provide a usable constraint on the opacity source.

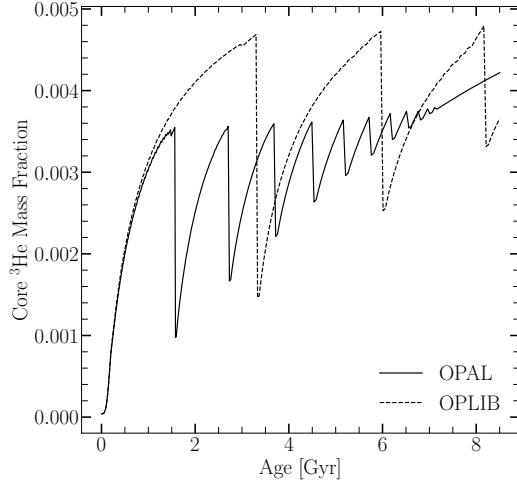


Figure 4.13: Core ^3He mass fraction for $0.3526 M_{\odot}$ models evolved with OPAL and OPLIB (within the Jao Gap's mass range for both). Note how the OPLIB model's core ^3He mass fraction grows at approximately the same rate as the OPAL model's but continues uninterrupted for longer.

4.9 Jao Gap connection to Magnatism

Chapter 5

Conclusions